TIME REVERSAL MATCHED FIELD PROCESSING: AN ANALYTICAL JUSTIFICATION

Amir Asif,   Qian (Amy) Bai,

Computer Science and Engineering
York University, Toronto, ON
asif@cse.yorku.ca

José M. F. Moura

Electrical and Computer Engineering
Carnegie Mellon University, Pittsburgh, PA
moura@ece.cmu.edu

ABSTRACT

The paper develops an analytical model to explain the phenomena of super resolution focusing achieved with time-reversal, matched field processing (TR/MFP). Our analytical model is based on multipaths introduced due to total internal reflections of the transmitted signal within a random medium. Under minor constraints, we show that the transfer function $\tilde{H}(\vec{y}_s \vec{x}_p \vec{y}_s, \omega)$ for the field observed at the location $\vec{y}_s$ of the scatterer contains a squared sinc term. Since multiplication of two similar sinc functions in the frequency domain is equivalent to the convolution of two rectangular functions with equal widths in the time domain, the result of convolution is a triangular function with a distinct peak at $\vec{y}_s$. In comparison, the transfer function $\tilde{H}(\vec{y}_s \vec{x}_p \vec{y}^o, \omega)$ for the field observed at an arbitrary site $\vec{y}^o$ includes multiplication of two sinc functions with different lobe widths, which leads to a trapezoidal function with no distinct peak in the time domain. In addition, the transfer function $\tilde{H}(\vec{y}_s \vec{x}_p \vec{y}^o, \omega)$ at any arbitrary site $\vec{y}^o$ contains a third sinc function, which peaks to its maximum value of $(2P + 1)$ at the location of the scatterer $\vec{y}_s$. This factor further amplifies super resolution focusing at the scatterer.

1. INTRODUCTION

The phenomena of super resolution focusing [1] observed in time-reversal, matched field processing (TR/MFP) [2] has been extensively used in a variety of scientific applications including under water acoustics, ultrasound eradication of cancerous cells in radiotherapy, and high signal to noise ratio reception (SNR) in cell phones. In general, TR/MFP includes the following steps.

- An active scatterer, embedded in an unknown medium, generates a probing pulse $f(t)$ into the random medium.

- A $(2P + 1)$ transducer array, placed within or outside the medium, records the waveforms at its transducer elements.

- The $(2P+1)$ elements time reverse the recorded waveforms and retransmit the time-reversed waves into the medium.

- The retransmitted waves focus strongly at the scatterer.

To intuitively explain the phenomenon of super-resolution focusing observed in TR/MFP, the paper considers a multipath propagation model, which is illustrated in Fig. 1. In our explanation, we assume that the geometric optics approximation to the wave equation is reasonable and strong reflections occur from the boundaries of the medium. Fig. 1 shows an active scatterer s, located at coordinate $\vec{y}_s = (x_s, y_s)$ on the right hand side of the channel, which
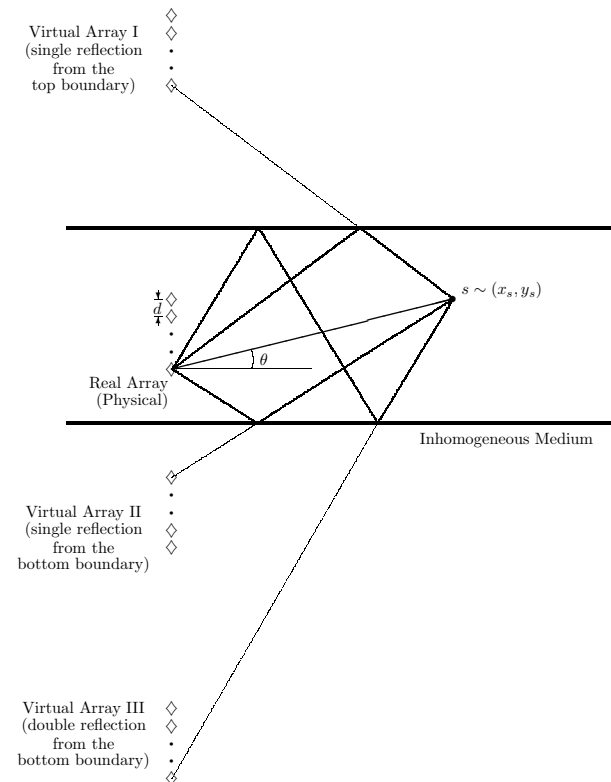
Fig. 1. Analytical multipath model used to explain super resolution focusing in time-reversal, matched field processing.

transmits the probing pulse $f(t)$. Several delayed and distorted versions of the probing pulse are received by the $(2P + 1)$ transducer array located on the left hand side of the channel. The transducer elements time reverse the received waveforms and transmit them back in the medium. Fig. 1 provides an intuitive explanation of why time reversal improves focusing and why the focusing is markedly increased when the multipath is richer. Each reflective multipath, considered in Fig. 1, can be treated to originate from an additional virtual array of $(2P + 1)$ transducer elements outside the boundaries of the medium under consideration. Richer multipaths with N reflections, therefore, lead to an increased number of $(2N + 1)$ arrays. Of these $(2N + 1)$ arrays, $2N$ arrays are virtual and lie outside the domain boundaries. This leads to a tighter refocusing than is possible with a single transducer array. The above
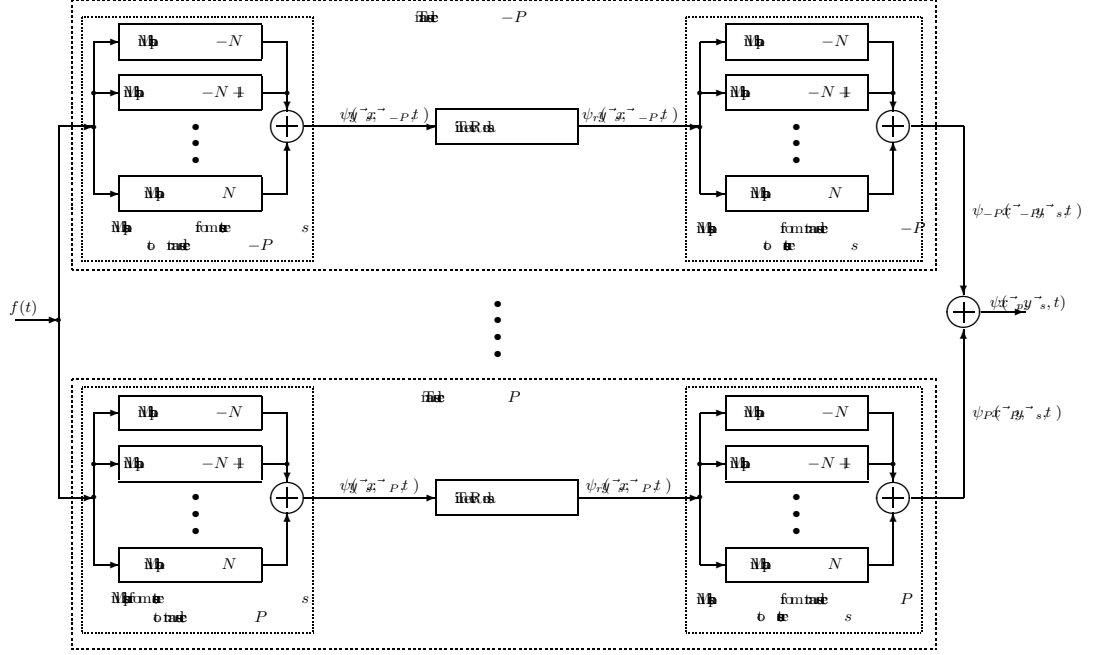
Fig. 2. Block diagram of the analytical multipath model used to represent the time-reversal, matched field processing.

description provides a flavor of the results that can be achieved in TR/MFP by exploiting the multipath structure. In this paper, we propose to provide a quantitative understanding of the practical gains afforded by TR/MFP and its limitations.

The paper is organized as follows. Section 2 introduces the multipath propagation model and estimates the propagation delay between multiple paths. In Section 3, we derive the transfer functions, also referred to as the ambiguity functions, for the field observed at the location of the scatterer and compare it to the transfer function for the field observed at any other arbitrary site. Section 4 provides intuitive explanation for the super resolution focusing in TR/MFP. Finally, Section 5 summarizes the paper.

2. ANALYTICAL MULTIPATH MODEL

The analytical model for the TR/MFP phenomena is shown in Fig. 2, where the probing pulse $f(t)$ is emitted omnidirectionally by the active scatterer s, located at coordinates $\vec{y}_s = (x_s, y_s)$, and is received by the transducer array. Each element p, $-P \leq p \leq P$, in the transducer array receives several delayed versions of $f(t)$ due to multipaths. The propagation of the probing pulse $f(t)$ from the scatterer s to the transducer element p, located at $\vec{x}_p = (x_p, y_p)$ is shown in the left column blocks of Fig. 2, where the waveform received by the transducer element p is denoted by $\psi(\vec{y}_s \vec{x}_p, t)$. Each transducer element time-reverses the received waveform $\psi(\vec{y}_s \vec{x}_p, t)$ as shown in the middle column of Fig. 2. The time reversed output of element p is given by $\psi_r(\vec{y}_s \vec{x}_p, t)$, which is retransmitted into the random medium. Each time-reversed waveform $\psi_r(\vec{y}_s \vec{x}_p, t)$, transmitted by transducer p, follows the same multipath model used in the forward transmission of the probing pulse $f(t)$ from the scatterer to the transducer array. The cumulative waveform $\psi(\vec{x}_p \vec{y}_s, t)$ is the sum of the waveforms $\psi_p(\vec{x}_p \vec{y}_s, t)$ received from the entire transducer array. The propa-

gation of the time reversed waveform from the transducer array to the scatterer is shown in the right-most column of Fig. 2. Next, we consider individual multipaths used in the forward and reversed transmissions. Fig. 3 illustrates the multipaths used in our analytical model to describe the propagation of the wave between the scatterer and a transducer element p with coordinate (x_p, y_p). In our discussion below, we consider five multipaths but the results are generalizable to a higher number $(2N + 1)$ of multipaths.

1. **Direct Path:** results due to the direct propagation of the field in a straight line between the scatterer s and the transducer element p. In Fig. 3(a), the direct path is shown as a solid bold line between sites s with coordinate (x_s, y_s) and p with coordinate (x_p, y_p). The distance $D_p^{(0)}$ traveled by the propagating wave from site s to site p using the direct path is approximated as

$$D_p^{(0)} = |x_s - x_p| + |y_s - y_p| \sin \theta_p, \qquad (1)$$

where θ_p is the angle between the direct path and the horizontal line joining transducer p with coordinate (x_p, y_p) with the projection of scatterer s with coordinate (x_s, y_s) onto site o with coordinate (x_s, y_p). The propagation delay of the field using the direct path is given by

$$\tau_p^{(0)} = \frac{|x_s - x_p| + |y_p - y_s| \sin \theta_p}{c}, \qquad (2)$$

where c is the propagation speed. The superscripts in Eqs. (1) and (2) indicate that the propagation distance and delay are calculated with respect to the direct path. In this paper, the direct path is referred to as $(n = 0)$ multipath, the top-boundary single-reflection path is referred to as $(n = 1)$ multipath, while the bottom-boundary single-reflection path is referred to as $(n = -1)$ multipath. Similarly, for the other superscripts used for the remaining multipaths.

2. **Top-Boundary Single-Reflection Path:** is shown as a solid bold line in Fig. 3(b), where the wave reaches the transducer after a single reflection at point u' from the top boundary. Expressed in terms of $D_p^{(0)}$, the distance $D_p^{(1)}$ traveled by the propagating wave following the top-boundary, single-reflection path is approximated as

$$D_p^{(1)} = D_p^{(0)} + 2y_s \sin \alpha_1, \qquad (3)$$

where α_1 is the angle of incidence of the propagating wave with the top boundary. The propagation delay of the wave using the top-boundary single-reflection path is given by

$$\tau_p^{(1)} = \tau_p^{(0)} + \frac{2y_s \sin \alpha_1}{c}. \qquad (4)$$

3. **Bottom-Boundary Single-Reflection Path:** is similar to the top-boundary single-reflection path except that the reflection takes place from the bottom boundary of the random medium. Based on Fig. 3(c), the distance $D_p^{(-1)}$ traveled by the signal using the bottom-boundary single-reflection path is approximated as

$$D_p^{(-1)} = D_p^{(0)} + 2(y_c - y_s) \sin \beta_1, \qquad (5)$$

where y_c is the width of the channel and β_1 is the angle of incidence of the propagating signal with the bottom boundary. The propagation delay for the signal using the bottom-boundary single-reflection path is given by

$$\tau_p^{(-1)} = \tau_p^{(0)} + \frac{2(y_c - y_s) \sin \beta_1}{c}. \qquad (6)$$

4. **Top-Bottom-Boundary Double Reflection Path:** is shown as solid bold lines in Fig. 3(d) and consists of three straight lines joining: (i) the site s with coordinate (x_s, y_s) with the reflection point u_1'' at the top boundary; (ii) u_1'' with the reflection point b_1'' at the bottom boundary; and (iii) b_1'' with the transducer element p with coordinate (x_p, y_p). The distance traveled by the signal using the top-bottom-boundary double reflection path is approximated as

$$D_p^{(2)} = \text{(distance between } p_b' \text{ and } s) + 2y_s \sin \alpha_2, \quad (7)$$

where α_2 is the angle of incidence of the propagating wave with the top boundary. In Eq. (7), the distance between p_b', the mirror image of the transducer element p located at $\vec{x}_p = (x_p, y_p)$ with respect to the bottom boundary, and the scatterer s is equal to the distance $D_P^{(-1)}$. Eq. (7) is, therefore, expressed as

$$D_p^{(2)} = D_p^{(-1)} + 2y_s \sin \alpha_2. \qquad (8)$$

which leads to the following propagation delay

$$\tau_p^{(2)} = \tau_p^{(-1)} + \frac{2y_s \sin \alpha_2}{c}. \qquad (9)$$

5. **Bottom-Top-Boundary Double Reflection Path:** is similar to the top-bottom-boundary double reflection path except that the first reflection takes place from the bottom boundary and is followed by the reflection from the top
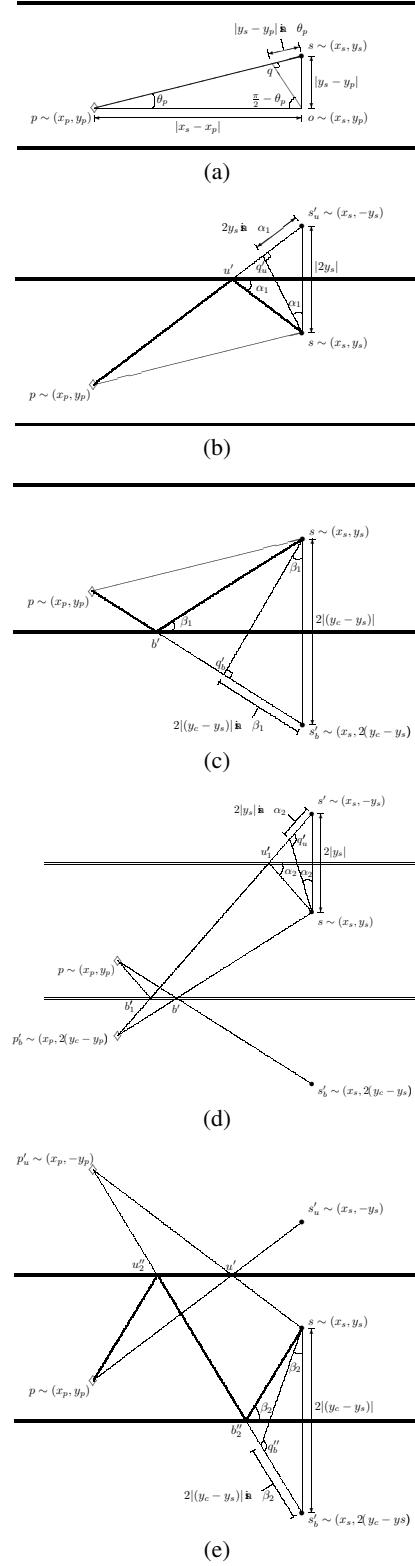

(a)

(b)

(c)

(d)

(e)

Fig. 3. Multipaths between scatterer s and array p in TR/MFP: (a) Direct path; (b) Reflection from top boundary; (c) Reflection from bottom boundary; (d) Reflection from top boundary followed by a second reflection from bottom; and (e) Reflection from bottom boundary followed by a second reflection from top.

boundary of the medium. Based on Fig. 3(e), the propagation distance is given by

$$D_p^{(-2)} = \text{(distance between } p'_u \text{ and } s) + 2(y_c - y_s)\sin\beta_2. \tag{10}$$

where β_2 is the angle of incidence of the propagation signal with the bottom boundary. Since the distance between sites p'_u, the mirror image of transducer element p with coordinate (x_p, y_p), and the location of the scatterer s is equal to the distance between p and s'_u, which is the mirror image of the scatterer with respect to the top boundary, the distance $D_p^{(-2)}$ is approximated as

$$D_p^{(-2)} = D_p^{(1)} + 2(y_c - y_s)\sin\beta_2. \tag{11}$$

which leads to the propagation delay

$$\tau_p^{(-2)} = \tau_p^{(1)} + \frac{2(y_c - y_s)\sin\beta_2}{c}. \tag{12}$$

In terms of the location of the scatterer s with coordinate (x_s, y_s) and transducer p with coordinate (x_p, y_p), the angles θ_p, α_i's, and β_i's used in Eqs. (1)-(12) are given by

$$\theta_p = \sin^{-1}\frac{|y_p - y_s|}{((x_s - x_p)^2 + (y_p - y_s)^2)^{0.5}} \tag{13}$$

$$\alpha_1 = \sin^{-1}\frac{y_0 + y_s}{((x_s - x_0)^2 + (y_0 + y_s)^2)^{0.5}} \tag{14}$$

$$\alpha_2 = \sin^{-1}\frac{2y_c - y_0 + y_s}{((x_s - x_0)^2 + (2y_c - y_0 + y_s)^2)^{0.5}} \tag{15}$$

$$\beta_1 = \sin^{-1}\frac{2y_c - y_0 - y_s}{((x_s - x_0)^2 + (2y_c - y_0 - y_s)^2)^{0.5}} \tag{16}$$

$$\text{and } \beta_2 = \sin^{-1}\frac{2y_c + y_0 - y_s}{((x_s - x_0)^2 + (2y_c + y_0 - y_s)^2)^{0.5}} \tag{17}$$

From the above discussion, the propagation distance of signal along multipath n in our analytical model may be generalized as

$$D_p^{(n)} = \begin{cases} D_p^{-(n-1)} + 2y_s\sin\alpha_n, & (n > 0) \\ D_p^{-(n+1)} + 2(y_c - y_s)\sin\beta_n, & (n < 0). \end{cases} \tag{18}$$

Dividing Eq. (18) with the propagation speed c, the propagation delays of the signals along multipath n are given by

$$\tau_p^{(n)} = \begin{cases} \tau_p^{-(n-1)} + \frac{2y_s\sin\alpha_n}{c}, & (n > 0) \\ \tau_p^{-(n+1)} + \frac{2(y_c - y_s)\sin\beta_n}{c}, & (n < 0). \end{cases} \tag{19}$$

3. AMBIGUITY FUNCTIONS

In this section, we derive the transfer functions, or the ambiguity functions, for the TR/MFP system.

Theorem 1 *At the location of the single scatterer $\vec{y}_s$, the transfer function $H(\vec{y}_s\vec{x}_p\vec{y}_s, \omega)$ of the TR/MFP in random medium, assuming a single scatterer, a $(2P+1)$ transducer element array, and $(2N+1)$ multipaths, is given by*

$$H(\vec{y}_s\vec{x}_p\vec{y}_s, \omega) \triangleq \frac{\Psi(\vec{x}_p\vec{y}^{-o}, \omega)}{F(-\omega)} = (2P+1)e^{j\omega T} \times \Bigg[C_n +$$

$$\frac{1}{2}\sum_{n_1=-N}^{N}\sum_{\substack{n_2=-N \\ n_2 \neq n_1}}^{N} a^{(n_1)}a^{(n_2)}\left(\frac{\sin\frac{3\omega(\tau_p^{(n_1)} - \tau_p^{(n_2)})}{2}}{\sin\frac{\omega(\tau_p^{(n_1)} - \tau_p^{(n_2)})}{2}}\right)\Bigg], \tag{20}$$

where C_n is a constant and is defined as

$$C_n = \sum_{n_1=-N}^{N}\left(a^{(n_1)}\right)^2 - \frac{1}{2}\sum_{n_1=-N}^{N}\sum_{\substack{n_2=-N \\ n_2 \neq n_1}}^{N} a^{(n_1)}a^{(n_2)}, \tag{21}$$

$a^{(n_1)}$ and $\tau_p^{(n_1)}$ are, respectively, the attenuation factors and the propagation delays along different multipaths n_1 from the scatterer $\vec{y}_s = (x_s, y_s)$ to the transducer element $\vec{x}_p = (x_p, y_p)$.

Proof: The field $\psi(\vec{y}_s\vec{x}_p, t)$, received by the p'th transducer element through the n'th multipath, is the signal $f(t)$ transmitted from the scatterer, which is delayed by the propagation time $\tau_p^{(n)}$ and attenuated by a factor of $a^{(n)}$. Considering $(-N \leq n \leq N)$ multipaths, the received signal at a transducer element p is given by

$$\psi(\vec{y}_s\vec{x}_p, t) = \sum_{n=-N}^{N} a^{(n)}f(t - \tau_p^{(n)}), \tag{22}$$

for $(-P \leq p \leq P)$. The superscript (n) denotes the number of the multipaths. Taking the Fourier transform of Eq. (22) gives

$$\Psi(\vec{y}_s\vec{x}_p, \omega) = F(\omega)\sum_{n=-N}^{N} a^{(n)}e^{-j\omega\tau_p^{(n)}}, \tag{23}$$

for $(-P \leq p \leq P)$. The Fourier transform $\Psi_r(\vec{y}_s\vec{x}_p, \omega)$ of the time reversal signal $\psi(\vec{y}_s\vec{x}_p, T - t)$ at transducer element p is

$$\begin{aligned}\Psi_r(\vec{y}_s\vec{x}_p, \omega) &= \Psi(\vec{y}_s\vec{x}_p, -\omega)e^{j\omega T} \\ &= e^{j\omega T}F(-\omega)\sum_{n=-N}^{N} a^{(n)}e^{j\omega\tau_p^{(n)}},\end{aligned} \tag{24}$$

for $(-P \leq p \leq P)$. The symbol T is the delay introduced in the time reversed signal $\psi(\vec{y}_s\vec{x}_p, t)$ to make it causal. The time reversed signal $\psi_r(\vec{y}_s\vec{x}_p, t)$ is back propagated into the random medium. The Fourier transform of the cumulative signal received by the scatterer from transducer element p through $(-N \leq n \leq N)$ multipaths is given by

$$\Psi_p(\vec{x}_p\vec{y}_s, \omega) = \Psi_r(\vec{y}_s\vec{x}_p, \omega)\sum_{n=-N}^{N} a^{(n)}e^{-j\omega\tau_p^{(n)}}. \tag{25}$$

Substituting the value of $\Psi_r(\vec{y}_s\vec{x}_p, \omega)$ from Eq. (24) gives

$$\Psi_p(\vec{x}_p\vec{y}_s, \omega) = e^{j\omega T}F(-\omega)\sum_{n_1, n_2=-N}^{N} a^{(n_1)}a^{(n_2)}e^{-j\omega(\tau_p^{(n_2)} - \tau_p^{(n_1)})}.$$

Considering the terms $(n_1 = n_2)$ and $(n_1 \neq n_2)$ in the double summation separately, the above equation simplifies to

$$\Psi_p(\vec{x}_p\vec{y}_s, \omega) = e^{j\omega T}F(-\omega)\Bigg[\sum_{n=-N}^{N}(a^{(n)})^2 \tag{26}$$

$$+ \frac{1}{2}\sum_{n_1=-N}^{N}\sum_{\substack{n_2=-N \\ n_2 \neq n_1}}^{N} a^{(n_1)}a^{(n_2)}\left(\frac{\sin\frac{3(\tau_p^{(n_1)} - \tau_p^{(n_2)})\omega}{2}}{\sin\frac{(\tau_p^{(n_1)} - \tau_p^{(n_2)})\omega}{2}} - 1\right)\Bigg],$$

which results in the system transfer function for a single transducer element p as

$$H_p(\vec{y}_s \vec{x}_p \vec{y}_s, \omega) = e^{j\omega T} \left[\sum_{n=-N}^{N} (a^{(n)})^2 \right. \tag{27}$$

$$\left. + \frac{1}{2} \sum_{n_1=-N}^{N} \sum_{\substack{n_2=-N \\ n_2 \neq n_1}}^{N} a^{(n_1)} a^{(n_2)} \left(\frac{\sin \frac{3(\tau_p^{(n_1)} - \tau_p^{(n_2)})\omega}{2}}{\sin \frac{(\tau_p^{(n_1)} - \tau_p^{(n_2)})\omega}{2}} - 1 \right) \right].$$

Taking $(2P+1)$ such transfer functions, one for each transducer element, it is straightforward to derive Eq. (20) of Theorem 1 from the above result. ∎

Corollary 1.1 *A special case of Theorem 1 is derived by assuming that: (1) the difference between the propagation delays along the multipath and the direct path is a factor of the delay along the direct path, and (2) the attenuations along multipaths other than the direct path are the same. Explicitly, we assume that*

$$\tau_p^{(n)} - \tau_p^{(0)} = |n|\tau_p, \text{ and } a^{(n_1)} = a^{(n_2)} = \frac{1}{2}a^{(0)}, \tag{28}$$

for $(-N \leq n_1, n_2 \leq N, n_1 \neq 0, n_2 \neq 0)$. The transfer function $H(\vec{y}_s \vec{x}_p \vec{y}_s, \omega)$ in Theorem 1 simplifies to

$$\tilde{H}(\vec{y}_s \vec{x}_p \vec{y}_s, \omega) = (2P+1)e^{j\omega T}(a^{(0)})^2 \left(\frac{\sin \frac{(N+1)\omega\tau_p}{2}}{\sin \frac{\omega\tau_p}{2}} \right)^2. \tag{29}$$

Note that the condition for the propagation delay in Eq. (28) is a direct consequence of Eq. (19). Following the procedure used in the derivation of Theorem 1, the transfer function of the TR/MFP system for any site $\vec{y}_o$ other than the location $\vec{y}_s$ of the scatterer is derived as follows. To save on space, we omit the proof here.

Theorem 2 *At any arbitrary observation site $\vec{y}_o$, the transfer function for the TR/MFP in random medium with a single scatterer, a $(2P+1)$ transducer element array, and $(2N+1)$ multipaths is*

$$H(\vec{y}_s \vec{x}_p \vec{y}_o, \omega) = \underbrace{\left(\frac{\sin \frac{(2P+1)d\omega(\sin\theta - \sin\theta^*)}{2c}}{\sin \frac{d\omega(\sin\theta - \sin\theta^*)}{2c}} \right)}_{\text{Term I}} e^{j\omega T}$$

$$\times \sum_{n_1=-N}^{N} \sum_{n_2=-N}^{N} a^{*(n_2)} a^{(n_1)} e^{-j\omega(\tau_p^{*(n_2)} - \tau_p^{(n_1)})}, \tag{30}$$

where the parameters with superscripts $(*)$ are measured with respect to the transducer element p and observation site $\vec{y}_o$. For example, $\tau_p^{*(n_2)}$ and $a^{*(n_2)}$ denote, respectively, the propagation delays and the attenuation factors along multipaths n_2 from transducer element $\vec{x}_p = (x_p, y_p)$ to the observation site $\vec{y}_o$. The angle θ^* is the angle between the direct path and the horizontal line joining transducer element (x_0, y_0) with the projection of the arbitrary site $\vec{y}_o$ onto the site (x_o, y_o). ∎

Corollary 2.1 *We derive the special case of Theorem 2 under assumption (28) for the propagation delay $\tau_p^{(n)}$ and attenuation $a^{(n)}$. Similar assumptions are also applied to the propagation delay $\tau_p^{*(n)}$ and attenuation $a^{*(n)}$ measured with respect to $\vec{y}_o$, i.e.,*

$$\tau_p^{*(n)} - \tau_p^{*(0)} = |n|\tau_p^*, \text{ and } a^{*(n_1)} = a^{*(n_2)} = \frac{1}{2}a^{*(0)}, \tag{31}$$

Multipath n	-2	-1	0	1	2
$a^{(n)}$	0.136ρ	0.309ρ	ρ	0.336ρ	0.136ρ
$a^{*(n)}$	0.170ρ	0.324ρ	3.520ρ	0.968ρ	0.170ρ

Table 1. Values of attenuations used in the analytical model. The constant ρ is obtained from the direct path and set to 0.055.

for $(-N \leq n_1, n_2 \leq N, n_1 \neq 0, n_2 \neq 0)$. The transfer function $H(\vec{y}_s \vec{x}_p \vec{y}_o, \omega)$ in Theorem 2 simplifies to

$$\tilde{H}(\vec{y}_s \vec{x}_p \vec{y}_o, \omega) = a^{*(0)} a^{(0)} e^{j\omega T} e^{\frac{j\omega N(\tau_p - \tau_p^*)}{2}} e^{j\omega(\tau_p - \tau_p^*)} \tag{32}$$

$$\underbrace{\left(\frac{\sin \frac{(2P+1)d\omega(\sin\theta - \sin\theta^*)}{2c}}{\sin \frac{d\omega(\sin\theta - \sin\theta^*)}{2c}} \right)}_{\text{Term II}} \underbrace{\left(\frac{\sin \frac{(N+1)\omega\tau_p}{2}}{\sin \frac{\omega\tau_p}{2}} \right)}_{\text{Term III}} \underbrace{\left(\frac{\sin \frac{(N+1)\omega\tau_p^*}{2}}{\sin \frac{\omega\tau_p^*}{2}} \right)}_{\text{Term IV}}.$$

3.1. Experimental Verification

To verify our analytical results, a controlled simulation is run on a $(70 \times 40)\lambda$ domain with an 8% randomness in the velocity profile $c(\vec{x})$ about $c = 1.5 \times 10^8$m/s. The 2D domain is discretized with a step size of $\Delta x = \Delta y = 0.25\lambda$, Mur boundary conditions [3] and wavelength $\lambda = 0.5$mm. The scatterer is located at $(53, 19.25)\lambda$, which emits the probing pulse

$$f(t) = -2\pi^2 v^2 (t - 1/v) e^{-\pi^2 v^2 (t - 1/v)^2}, \ 0 \leq t \leq 0.7\mu s, \tag{33}$$

where $v = \frac{c}{\lambda}$ is the central frequency, λ is the wavelength, which is given by 0.5 mm, and t denotes time. The probing pulse generates a 2D field $\psi(\vec{y}_s \vec{x}_t)$ that propagates within the random medium according to the wave hydrodynamic equation [4] as

$$\Delta\psi(\vec{y}_s \vec{x}_t) - \frac{1}{(c(\vec{x}))^2} \frac{\partial^2 \psi(\vec{y}_s \vec{x}_t)}{\partial t^2} = -f(t)\delta(\vec{x} - \vec{y}_s). \tag{34}$$

A 21 element transducer array, located at $(15, 20 + (p-1)/2)\lambda$, for $(-10 \leq p \leq 10)$, receives the propagated waves and time-reverses the waveforms. Each element retransmits the signal into the medium. In Fig. 4, we compare the spectrum of the fields $\psi(\vec{x}_p \vec{y}_s, t)$ observed at the location $\vec{y}_s = (53, 19.25)\lambda$ of the scatterer and an arbitrary observation site $\vec{y}_o = (35, 12.5)\lambda$ obtained from the experiment with the corresponding analytical fields derived from Eq. (20) in Theorem 1 and Eq.(30) in Theorem 2 with the number of multipaths $(2N+1)$ set to 5. In our model, the attenuation within the random medium n is assumed to be inversely proportional to the square of the length of the multipath and are specified in Table 1. The plots in Fig. 4 show that the fields derived from our analytical model are fairly good approximations of the field observed in the experimental simulation. With an increase in the number of multipaths, the approximations improve even further. We also observe that the maximum height of the field at the location of scatterer is at least 5 to 6 times stronger than that of the field observed at site $(35, 12.5)\lambda$, which verifies the refocusing phenomena observed in TR/MFP.

4. EXPLANATION OF THE REFOCUSING PHENOMENA

In this section, we use Theorems 1 and 2 to explain the refocusing phenomena in TR/MFP. Note that Eq. (20) is a special case of
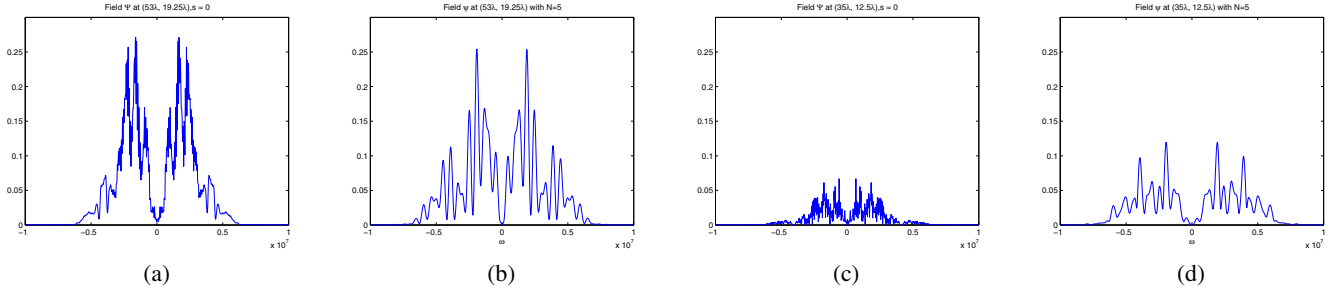
Fig. 4. Comparison of fields $\psi(\vec{x}_p y\vec{\,}_s, t)$ obtained experimentally versus the corresponding fields derived analytically. (a) Experimentally observed field at the scatterer located at $y\vec{\,}_s = (53, 19.25)\lambda$. (b) Same as (a) except that the field is computed analytically using Theorem 1. (c) Experimentally observed field at site $y^{\rightarrow o} = (35, 12.5)\lambda$. (d) Same as (c) except that the field is computed analytically using Theorem 2.

Eq. (30) for the limiting case $\theta = \theta^*$. Applying the L'Hopital's rule, Term I in Eq. (30) reduces to

$$\lim_{\theta \to \theta^*} \frac{\sin \frac{(2P+1)d\omega(\sin\theta - \sin\theta^*)}{2c}}{\sin \frac{d\omega(\sin\theta - \sin\theta^*)}{2c}} = (2P+1), \qquad (35)$$

while the double summation in Eq. (30) can also be expressed as a sum of C_n and an additional term shown in Eq. (20). Comparing the relative strength of the transfer functions, we observe that the transfer function at the location of the scatterer is greater than the transfer function at any arbitrary site. The magnitude of Term I in Eq. (30) is relatively smaller than its peak value of $(2P+1)$ in Eq. (20). This peak value of the sinc function in Eq. (20) leads to a stronger signal, which explains why refocusing is strongest at the location of the scatterer than at any other site.

A second observation made from Eqs. (20) and (30) is that the magnitudes of the transfer functions are dependent on the number $(2N+1)$ of multipaths in the random medium. The transfer functions $H(\vec{y}_s x\vec{\,}_p y\vec{\,}_s, \omega)$ and $H(\vec{y}_s x\vec{\,}_p y^{\rightarrow o}, \omega)$ have higher magnitudes if the number of multipaths is increased. Since multipaths arise from total internal reflections, which are stronger in random medium, therefore, Eqs. (20) and (30) demonstrate stronger refocusing in random medium as compared to homogeneous medium.

The explanation for super resolution refocusing is obtained from Corollaries 1.1 and 2.1. There are two differences in the simplified transfer functions $\tilde{H}(\vec{y}_s x\vec{\,}_p y\vec{\,}_s, \omega)$ and $\tilde{H}(\vec{y}_s x\vec{\,}_p y^{\rightarrow o}, \omega)$.

1. The first difference results from Term II in $\tilde{H}(\vec{y}_s x\vec{\,}_p y^{\rightarrow o}, \omega)$ that has the maximum value of $(2P+1)$ in $\tilde{H}(\vec{y}_s x\vec{\,}_p y\vec{\,}_s, \omega)$. This results in a stronger field at the location of the scatterer than at any other observation site.

2. The second difference results from Terms III and IV in transfer function $\tilde{H}(\vec{y}_s x\vec{\,}_p y^{\rightarrow o}, \omega)$. At the location of the scatterer, the propagation delays $\tau_p = \tau_p^*$ in Terms III and IV resulting in a sinc^2 term in $\tilde{H}(\vec{y}_s x\vec{\,}_p y\vec{\,}_s, \omega)$. Multiplication of two sinc functions in the frequency domain is equivalent to convolution of two rectangular functions in the time domain. In $\tilde{H}(\vec{y}_s x\vec{\,}_p y\vec{\,}_s, \omega)$, sinc functions have the same lobe widths, therefore, the result of the time domain convolution is a triangular function with a prominent peak at the location of the scatterer. On the other hand, Terms III and IV in Eq. (30) have different lobe widths, therefore, the result of convolution in the time domain is a trapezoid, which is flat in the middle region. Since the sinc functions have the same energy in the frequency domain,

the peak observed in the impulse response corresponding to $\tilde{H}(\vec{y}_s x\vec{\,}_p y\vec{\,}_s, \omega)$ is higher in magnitude than the maximum value of the trapezoid in the impulse response of $\tilde{H}(\vec{y}_s x\vec{\,}_p y^{\rightarrow o}, \omega)$. This is the second factor that leads to stronger refocusing at the location of the scatterer.

5. SUMMARY

To explain super resolution focusing in TR/MFP, the paper presented an analytical multipath model that assumed geometric optics approximation with strong total internal reflections from the boundary of the random medium. We derived the ambiguity functions for TR/MFP at the location $y\vec{\,}_s$ of the scatterer and at any other observation site $y^{\rightarrow o}$. The transfer function $\tilde{H}(\vec{y}_s x\vec{\,}_p y\vec{\,}_s, \omega)$ for the field observed at the scatterer contains a squared sinc term, which is equivalent to convolution of two rectangular functions in the time domain. The resulting impulse response is a triangular function with a distinct peak at the scatterer. In comparison, the transfer function $\tilde{H}(\vec{y}_s x\vec{\,}_p y^{\rightarrow o}, \omega)$ for the field observed at any other arbitrary site includes multiplication of two sinc functions with different lobe widths, which leads to a trapezoidal function, with no distinct peak, as its impulse response. In addition, $\tilde{H}(\vec{y}_s x\vec{\,}_p y^{\rightarrow o}, \omega)$ contains a third sinc function, which peaks to its maximum value of $(2P+1)$ at the scatterer. This term further amplifies super resolution focusing at the scatterer. Though not presented here, the analytical model has been used to derive robust algorithms [5] for detecting the number and location of the embedded scatterers.

6. REFERENCES

[1] L. Borcea, G. Papanicolaou, C. Tsogka, and J. Berryman "Imaging and Time Reversal in Random Medium," *Inverse Problems*, vol. 18, 2002, pp. 1247-79.

[2] M. Fink and C. Prada, "Accoustic Time-Reversal Mirrors: Topic Review," *Inverse Problems*, vol. 17, 2001, pp. R1-R38.

[3] G. Mur, "Absorbing Boundary Conditions for the Finite Difference Approximation of the Time-Domain Electromagnetic Field Equations," *IEEE Trans. Electromagnetic Compaction*, vol. 23, 1981, pp. 377-82.

[4] G. Barton, "Element of Green's Functions & Propagation: Potentials, Diffusion, and Waves," Clarendon Press, 1989, pp. 71.

[5] Q. Bai, "Robust Target Detection Algorithms for Time Reversal Matched Field Processing," M.S. Thesis, York Univ., 2005.